Tracing immune cells around biomaterials with spatial anchors during large-scale wound regeneration

Authors: Yang Yang[12]†, Chen-yu Chu[1]†, Yi Man[1]†, Li Liu[1]†, Chen-bing Wang[1], Yi-li Qu[2]*

Affiliations:

[1] Department of Oral Implantology & State Key Laboratory of Oral Diseases and National Clinical Research Center for Oral Diseases, West China Hospital of Stomatology, Sichuan University; Chengdu 610041, China.

[2] Department of Prosthodontics & State Key Laboratory of Oral Diseases and National Clinical Research Center for Oral Diseases, West China Hospital of Stomatology, Sichuan University; Chengdu 610041, China.

* Corresponding author. Email: qqyili@126.com (Y.L.Q.)

† These authors contributed equally to this work

Abstract:

Inevitable skin scarring devoid of dermal appendages bring about unfavorable effects on both aesthetic and physiological functions. Here we offered an available method for large-area wound regeneration using biodegradable Aligned extracellular matrix (ECM) scaffold. Accelerating wound coverage and enhanced hair follicle (HF) neogenesis were observed with the implantation of biomaterials. Multimodal analysis during wound regeneration provides a unique lens through which we can explore the foreign body responses (FBR) around biomaterials. First, we identified cell heterogeneity in responses to ECM scaffolds using single-cell RNA sequencing. Next the spatial anchor highlighted preferential recruitment of T cells around biomaterials colocalized with hair follicle precursor cells. Reconstruction of signaling pathways suggested the pro-regenerative effect of the adaptive immune systems on HF neogenesis. Immunodeficient mice lacking mature T lymphocytes lost the ability to activate papillary fibroblast as well as stimulate

26 HF regeneration, validating the potential therapeutic effect of the adaptive immune system
27 activated by biomaterials. In conclusion, this study provided the further understanding of the
28 FBR and facilitate the design of immunoregulatory biomaterials for biomedical application in the
29 future.

30 **Introduction:**

31 After severe skin damage, resulting scar usually contain dense extracellular matrix (ECM) fibers
32 devoid of hair follicle (HF) and sebaceous gland (SG), which lack sensation and endocrine
33 function as well as flexibility of normal skin[1]. As a result, there is an urgent need to explore the
34 key mechanisms stimulating HF regeneration in skin repair.

35 In fact, tissue regeneration mediated by immunoregulatory biomaterials is emerging as a
36 perspective strategy in tissue engineering[2,3]. Biological cues can be integrated into a polymer
37 scaffold to mimic the native ECM, which guides tissue regeneration[4,5]. Upon materials
38 implantation, the FBR process initiates with an immune response. It has been shown that
39 modulating FBR by adjusting biomaterials characteristic may create a desired biological
40 response to mobilize stem cells or stimulate specific cell proliferation [4,5]. Previous study reported
41 that the Aligned nanofibers scaffold with an immunomodulatory effect in accelerating small skin
42 wound (diameter = 0.6cm) healing[6,7]. Since the delayed wound closure and susceptibility to
43 infection in large scale defects[8], the pro-regenerative effect of ECM scaffold in large wound
44 needs further evaluation. What's more, as immune cells are recruited into the scaffold to create a
45 desirable microenvironment for cell adhesion, proliferation, and tissue reconstruction, the
46 interactions between immune cells and cutaneous cell become more complex.

47 Currently, high resolution technique such as single-cell RNA sequencing (scRNA-seq)[6,9,10] has
48 been applied to identifies cell subpopulations in implantation model but lack the information of
49 spatial distribution. Development in spatial transcriptomics (ST) has enabled the assessment of

50 gene expression at spatial resolution[11], which has been applied to the study of cancer[12 13], liver[14],
51 and brain tissue[15] to detect the regional cellular communication. The wound healing model with
52 implanted biomaterials provide an ideal method to understand the FBR and probe the role of
53 immune system in tissue regeneration. To our knowledge, multiomic approaches, including
54 scRNA-seq and ST, were firstly applied to trace spatial heterogeneity in the biomaterial-
55 mediated wound healing process in this study. Here we unveiled the cell composition around the
56 ECM scaffold in both wildtype and immunodeficient mice to anchor the key role of T cells in HF
57 regeneration, which would help optimize the existing biomaterial constructs and provide feasible
58 strategies for the design of novel immunoregulatory products in tissue engineering for
59 biomedical use.

60 **Results**

61 **Enhanced HF neogenesis in scaffold-implanted wounds with activation of the adaptive**
62 **immune system**

63 To minimize wound contraction by the panniculus carnosus of rodents and induce scar large
64 enough to observe[16],we created a large area splinted full-thickness wound healing model in
65 C57BL/6 mice to investigate whether a further regenerative phenomenon was observed in ECM
66 scaffold-treated wounds. The workflow for evaluating large wound healing is summarized in Fig.
67 1a. We placed ECM scaffolds below the large wound (diameter = 1.5 cm) in the ECM_LW
68 group, while the Ctrl_LW group received no biomaterials (Fig. 1b). Wound coverage was faster
69 in the ECM_LW group on day 7 (Fig. 1 c, d), and the ECM_LW group also had a smaller gap
70 width on day 7 and day 14 (Fig. 1e,f). Immunofluorescence (IF) staining for cytokeratin 5 (Krt5)
71 and cytokeratin 10 (Krt10) showed that keratinocytes crawled around the biomaterials, and the
72 ECM_LW group owned a larger area of neo-epithelium (Fig. 1h).

73 Rare capability of adult mammals for limited HF regeneration[17,18] was observed in Ctrl_LW
74 group: there were limited HF neogenesis restricted in wound center since the POD21. In
75 comparison, we observed that the ECM_LW group recapitulated the normal skin architecture
76 with an equivalent number of mature HF on POD28 (Fig. 1g). The outline of HF morphogenesis
77 could be recognized in Fig 1e, with the first appearance in the hair germ stage on POD7, they
78 gradually grew into a bulbous-peg structure on POD21, and fully regenerated with mature hair
79 shafts, dermal papillae, sebaceous glands, and bulges on POD28. Of note, the ECM membrane
80 implanted in the large wound did not trigger any obvious fibrous capsule and exhibited an
81 appropriate degradation rate in vivo. We observed degrading fragments on POD14, and there
82 were no visible particles remaining on POD28 (Fig. 1e). The excellent biocompatibility and
83 degradability of the membrane could prevent the risk of immune rejection and secondary surgery
84 in further clinical applications.
85 To explore the underlying mechanism, Bulk-tissue RNA-seq (bulk-seq) analysis was conducted
86 for two groups harvested on day 7 (n =3 for each group) .We noticed that the ECM_LW group
87 showed increased enrichment of genes involved in hair follicle development along with T cell
88 differentiation (Fig. 1i). Immunohistochemistry (IHC) staining and flow cytometry confirmed
89 increased T-cell infiltration from ECM_LW group in early phase (Fig. 1 j, k). In Ctrl_LW group,
90 IF staining showed the accumulation of CD3-expressing T cells and Lgr5-espressing hair follicle
91 stem cells (HFSC) limited in wound center on day7, day 14 and day 21 (Extended Data Fig. 1a-
92 c), whereas biomaterials resulted in the robust recruitment of T cells and HFSC within and
93 around the scaffold on day7 and day14 (Extended Data Fig. 1a-c).
94 **A single-cell atlas of the biomaterials tissue microenvironment**
95 To explore the spatial characteristics of single cells during wound healing, we applied ST and
96 scRNA-seq to compare the spatial gene expression profiles between two groups (Fig. 2a). At first,

97 to explore the cell composition in biomaterial-treated wound, we isolated cells from the
98 ECM_LW and Ctrl_LW samples and applied them to the 10x scRNA-seq platform (Extended
99 Data Fig. 2a). After cell filtering, 31,740 single-cell transcriptomes were included in the final
100 dataset (20,312 for the ECM_LW group and 11,428 for the Ctrl_LW group). Unsupervised
101 clustering using Seurat categorized the cells into 10 main classes of cells. The composition of
102 each cell cluster was listed so that the proportion of cells from two groups could be identified
103 across all cell clusters (Extended Data Fig. 2b).
104 In previous report, HF neogenesis occurs through the migration of epithelial HFSC or hair
105 follicle progenitor (HFP) to the wound center and form the placodes to activate papillary
106 fibroblast (PF) fate specification into dermal condensate (Dc)[17,19,20]. The heterogeneity of
107 keratinocyte and fibroblast subclusters of this dataset corresponded with the healing outcomes of
108 two groups. Firstly, for subclustering analysis of keratinocyte (Fig. 2b), the higher proportion of
109 Krt5^{+}Krt14^{+} interfollicular epidermal basal cell[1] (IFEB[1]) and Krt10^{+}Krtdap^{+} interfollicular
110 epidermal differentiated cell[1] (IFED[1]) were observed in the ECM_LW group, supporting more
111 neo-epithelium proliferation in the presence of scaffolds. In addition, we found the higher
112 proportion of Krt25^{+}Krt28^{+}Krt27^{+} hair follicle progenitor[1] (HFP[1]) [6] and Crip1^{+}Lrig1^{+}Lgr5^{+} hair
113 follicle stem cell[1] (HFSC[1])[21] in ECM_LW group, which served enough epithelial resources for
114 HF reconstruction. Next, we defined two fibroblasts and six fibroblast-like cells subclusters
115 based on defined markers published before[6,19,22,23] (Fig. 2c). In accordance with previous
116 report[19,24], the major initial wave of dermal repair in Ctrl_LW group was mediated by the lower
117 lineage fibroblast including Mfap4^{+} Cd34^{+} lipo-fibroblast[1] (LF[1]) and Dpp4^{+}Mgp^{+}Gpx3^{+}Plac8^{+}
118 reticular fibroblast[1] (RF[1]) , which was respectively related to hypodermis adipocytes formation
119 and dermis collagen fibril organization in gene ontology (GO) enrichment analysis (Extended
120 Data Fig. 3a). In contrast, there were more upper lineage PF in biomaterial-implanted wound.

121 The PF in this dataset consisted of 2 subclusters including PF1[1] (Runx1+Inhba+)[22] and PF2[1]
122 (Notch1+Prdm1+)[25], both of which were believed to have the capacity to support HF initiation
123 (Extended Data Fig. 3a). For fibroblast-like subclusters, we observed higher proportion of
124 (Papp2^{+}Corin^{+}) dermal papilla[1] (DP[1]) cells in ECM_LW group, which resided in the mature HF
125 base in normal skin. Remarkably, we identified the Smad3^{+}Lef1^{+}Krt17^{+} dermal condensate[1] (Dc[1])
126 cell[20] in this dataset. Derived from PF, the Dc was believed to be the origin of DP[20,26]. In
127 embryologic HF morphology, Dc is acting as the signaling niches to stimulate epithelial placode
128 growth[20], and thus promote HF morphogenesis. Since approximate 90% of Dc[1] were from
129 ECM_LW group, as well as significantly higher proportion of PF1[1] and PF2[1], which might
130 provide enough mesenchymal component for the subsequent HF formation in biomaterial
131 implanted group too.
132 For Ptprc+ immune micro-environment, most myeloid cells owned the lower proportion in
133 ECM_LW group (Extended Data Fig. 2b). Firstly, as the first responding immune cells acting as
134 the critical mediators of innate immune system, neutrophils are necessary for the recruitment and
135 differentiation of monocytes[27]. Four neutrophil subsets including Il1b^{+}Retnlg^{+} peripheral blood
136 neutrophil[1] (PBN[1]), Il1a^{+}Tnf^{+} neutrophil1[1] (Neu1[1]), Lrg1^{+}Il1r2^{+} neutrophil2[1] (Neu2[1]),
137 Ccl9^{+}Rgs1^{+} neutrophil3[1] (Neu3[1]) were identified in our dataset (Extended Data Fig. 4a). Neu3[1]
138 was the only subsets owned a higher proportion in ECM_LW group and showed gene
139 enrichment in leukocyte migration and Th17 cell differentiation. Dendritic cell (DC) was
140 classified into two subclusters including Krt5^{+}Krt14^{+} langerhans cell[1] (LC[1]) and Cd86^{+} monocyte
141 derived dendritic cell[1] (MDC[1]) (Extended Data Fig. 4b). Kyoto Encyclopedia of Genes and
142 Genomes (KEGG) enrichment analysis showed that LC[1] and MDC[1] respectively related to
143 phagosome and antigen presentation. There was no obvious difference in the proportion of DC
144 subsets between the two groups. Monocytes and macrophages were of vital importance in

145 orchestrating biomaterial related FBR and tissue regeneration[28]. Three subsets of macrophages
146 including Ccl8^{+}Folr2^{+}C1qa^{+}Mrc1^{+} anti-inflammatory macrophages^{1} (AIM^{1}),
147 Mmp12^{+}Arg1^{+}Inhba^{+}Nos2^{+} pro-inflammatory macrophages^{1} (PIM^{1}) and Ly6c2^{+}Plac8^{+}Cytip^{+}H2-
148 Eb1^{+} monocytes^{1} (Mono^{1}) were determined. The ECM_LW group contributed to a lower
149 proportion of all three subsets, suggesting that the scaffold might play a role in the reduction of
150 macrophage infiltration at the proliferative stage (Fig. 2d).
151 T cells were the only immune cell which owned a higher proportion in ECM_LW group
152 (Extended Data Fig. 2b), and genes related to T cells (Il7r, Areg and Tubb5) were substantially
153 higher expressed by the ECM_LW group (Extended Data Fig. 2d), suggesting the activation of
154 adaptive immune system induced by biomaterials. Subclustering of T cells resulted in seven
155 subsets including Cd8b1^{+} cytotoxic T cell^{1} (CTL^{1}), Tyrobp^{+}Nkg7^{+}Xcl^{+} nature killer cell^{1} (NKT^{1}),
156 Il17a^{+}Il17f^{+} T helper17^{1} (Th17^{1}), Foxp3^{+} T regulatory cell^{1} (Treg^{1}), Trdv4^{+}Cd7^{+}Ctsw^{+} γδT cell^{1}
157 (Tγδ^{1}), Gata3^{+}Il5^{+} T helper2^{1} (Th2^{1}) and Bcl11a^{+}Id3^{+}Notch1^{+} innate lymphoid cell^{1} (ILC^{1}) based
158 on markers from published research[29,30]. Derived from common lymphoid progenitors, ILCs
159 mirror αβ T cell subtypes functionality responding to local signals but lack antigen-specific
160 receptors. In skin, tissue resident ILCs play key roles in barrier integrity, inflammatory response
161 initiation, and immunological response modulation in wound repairing[30-33]. Correlation analysis
162 showed that ILC^{1} was highly correlated with CTL^{1} (Extended Data Fig. 3c). Remarkably, skin-
163 resident ILC^{1} in our dataset possessed a tissue specific transcriptional profile that co-expression
164 genes related to T cell functionality (Cd3d^{+}Klf4^{+}Fst^{+}Itga6^{+}) and HF morphology
165 (Wnt4^{+}Sox9^{+}Fgfr2^{+}). Gene enrichment analysis showed the ILC was enriched in bacterial
166 invasion of epithelial, leukocyte transendothelial migration as well as Wnt signaling pathway
167 (required in hair follicle regeneration[17]) (Extended Data Fig. 3b), suggesting that ILC^{1} might
168 initiate HF neogenesis by balancing reparative and pro-inflammatory functions[34].

169 **Discovery of spatial heterogeneity around biomaterials**

170 To explore the spatial characteristics of cell heterogeneity in scaffold-implanted wounds, we
171 applied ST analyze the spatial gene expression profiles. Anatomical structures were identified in
172 the ST sections (Fig. 3a). Based on the gene enrichment analysis of ST, the ECM_LW sample
173 showed up-regulated gene expression in hair follicle morphogenesis as well as adaptive immune
174 response (Fig. 3b). The spatial feature plot illustrated keratinocytes crawling around the
175 implanted biomaterials (Fig. 3c). Moreover, the distribution of PF[1] (HF-related) was enlarged in
176 the ECM_LW group (Fig. 3d). In contrast, lower lineage fibroblasts RF[1], were significantly
177 reduced, suggesting different healing outcomes of two groups. Generally, HF formation does not
178 start until several days after wound closure (POD14–21) in large wounds without implantation[17].
179 In the ST profiling of the ECM_LW group on POD7, we identified the initial structure of the HF
180 composed of Krt28^{+} HFP in the neo-epidermis and Twis2^{+} Dc aggregation beneath the dermis
181 (Fig. 3e), which highlighted the early HF formation signature in the ECM_LW group at the
182 spatial gene expression level (Fig. 3f).

183 To explore the scaffold-induced immune microenvironment, we integrated marker genes of
184 immune cells (defined in Fig. 2) with ST profiling. We noticed the obvious aggregation of
185 monocyte-macrophage (MAC) and T cell subclusters surrounding the biomaterial (Fig. 3g,h).
186 Notably, we observed the accumulation of tissue-resident ILC[1] in the epithelium and granulation
187 tissue in the ECM_LW group (Fig. 3h). ILCs that co-expressed genes related to the adaptive
188 immune response as well as hair follicle development may be critical regulators initiating HF
189 formation.

190 **Prediction of critical signaling patterns between spatially co-localized cell populations**
191 **around the biomaterial**
192 Based on the multimodal profiling, we observed the higher proportion (Fig. 4a) and overlapping
193 distribution of T cells and HF precursor cells (Fig. 4b) in the ECM_LW group, which implied a
194 potential cellular communication among them. Next, we applied CellChat to predict the cell-cell
195 communication patterns between EMC_LW and Ctrl_LW. The heatmap shows the overall
196 signaling strength of the ligand-receptors in the Ctrl_LW and ECM_LW groups (Fig. 4c).
197 Adaptive immune system-related pathways, including MHC-II, were further activated in
198 ECM_LW. In addition to IL6, key signaling pathways in embryonic HF development such as
199 fibroblast growth factor (FGF) [20], NOTCH [35], and KIT [36] were also upregulated in the ECM_LW
200 group. The critical functions of NOTCH [35] , pleiotrophin (PTN), and midkine (MK) [36] in skin
201 morphology have been emphasized previously. Consistent with the gene expression profile in
202 single cell level, adaptive immune cells and HF precursor cells were enriched with interacting
203 receptor/ligand gene partners, including Jag1-Notch2, Mdk-(Sdc1 or Itgb1), and Ptn-(Itgb1or
204 Sdc1) in ST profiles (Fig. 4 d, e). Based on analysis above, adaptive immune cells might
205 modulate HF precursor cell growth through these pathways, thus facilitating HF formation.
206 **Adaptive immune system was required for the skin regeneration mediated by ECM**
207 **scaffold**
208 To determine the role of adaptive immune system in HF regeneration, we placed ECM scaffolds
209 in the dorsal skin of immunodeficient C57Bl/6 (B6.129-Rag2tm1) mice, which lacked mature T
210 lymphocytes and innate lymphoid cells [37,38] (Fig. 5 a, b). We noticed that the wound closure rate
211 was delayed on day7 (Fig. 5c-5e), and regeneration of HF was scarce (Fig. 5c, f) on day 28 in
212 Rag2$^{-/-}$ mice. Compared to wild type (WT) mice, Rag2$^{-/-}$ group still possess a myeloid
213 recruitment ability, but no visible accumulation of T cell around biomaterials was observed (Fig.

214 5 g , h). Next, we further explored the differences in cell composition and spatial gene expression
215 between WT and Rag2$^{-/-}$ mice using scRNA-seq (Extended Data Fig. 5a). Unsupervised
216 clustering categorized the cells into nine clusters based on gene expression (Extended Data Fig. 5
217 b, c). Firstly, subclustering analysis of mesenchymal cell identified two fibroblast-like cell and
218 five fibroblast cell subsets (Fig. 5i). In accordance with the HF regeneration outcomes, the Rag2^{-}
219 $^{/-}$ group reduce the proportion of PF^{2} (related to HF development) but improve the number of RF^{2}
220 (related to collagen deposition) and LF^{2} (related to collagen deposition and angiogenesis). For
221 immune microenvironment, the Rag2$^{-/-}$ samples recruited less adaptive immune cells
222 (Cd3g^{+}Cd7^{+} T cells) and more innate immune cells (Lyz2^{+}C1qb^{+} monocytes and macrophages)
223 than the WT group (Extended Data Fig. 5b). T cell related genes such as Areg, Trdc and Rgs2
224 were down-regulated in Rag2$^{-/-}$ samples (Extended Data Fig. 5d). The proportion of neutrophil
225 and dendritic cell subsets was basically equilibrium between the two groups (Extended Data Fig.
226 6a,b). Subclustering of macrophages resulted in four subsets, which were PIM^{2}, AIM^{2}, Mono^{2},
227 and MDC^{2} (Fig. 5j). Rag2$^{-/-}$ samples showed the lower number of Mono^{2} (related to T helper
228 cell differentiation), but improve the recruitment of PIM^{2}, AIM^{2}, and MDC^{2}. Subclustering of T
229 cells resulted in seven subsets (Fig. 5k), the Rag2$^{-/-}$ groups contributed to less T cells in most
230 subsets except NKT^{2} (related to natural killer cell mediated cytotoxicity) and Th2^{2}, indicating the
231 reduction of adaptive immune systems in Rag2$^{-/-}$ group.
232 To explore the spatial characteristics of cell heterogeneity in immunodeficient mice, we also
233 applied ST analyze the spatial gene expression profiles. Anatomical structures could be
234 identified in the ST sections (Fig. 6a). Based on the gene enrichment analysis of ST, the Rag2$^{-/-}$
235 sample down-regulated gene expression in hair follicle morphogenesis but improve the genes
236 related to collagen fibril organization (Fig. 6b). Compared to WT samples, the distribution of PF^{2}
237 (HF-related) was reduced. Lower lineage fibroblasts RF^{2} and LF^{2} were significantly enlarged

238 instead, corresponding with the healing outcome of Rag2$^{-/-}$ groups. To compare the scaffold-
239 induced immune microenvironment, we integrated marker genes of immune cells (defined in Fig.
240 5 j, k) with ST profiling. We noticed the aggregation of monocyte-macrophages (MAC)
241 surrounding the biomaterial in both group (Fig. 6d). The expression of the T cell subsets were
242 dramatic declined(Fig. 6e), indicating the reduction of adaptive immune system in Rag2$^{-/-}$ group.

243 **Biomaterials facilitate de novo HF regeneration despite of wound size**

244 To detect any differences in wound healing between small and large wounds treated with
245 biomaterials, we repeated the experiment with small (diameter=0.6 cm) and large (diameter=1.5
246 cm) full-thickness wounds implanted with biomaterials (Fig. 7 a, b). Consistent with the
247 ECM_LW group, the scaffold implanted in the small wound (ECM_SW) did not trigger an
248 obvious FBR fibrous capsule and had a rapid degradation rate (Fig. 7 c, d). Histological sections
249 of ECM_SW tissue revealed clear signs of enhanced HF reconstruction too (Fig. 7 c, f). Based
250 on bulk-seq profiling (n=3 for each group), heatmaps showed insignificant changes in HF-related,
251 adaptive immune response, or innate immune response gene expression between the two groups
252 (Extended Data Fig. 7a). IHC staining for CD3 and CD68 confirmed similar infiltration levels of
253 T cells and monocyte-macrophages surrounding the scaffold (Fig. 7e).

254 We further explored the differences in immune cell composition using scRNA-seq and ST (Fig.
255 7 g, h). Feature plot showed the aggregation of Ptprc+ immune cells (Fig. 7i). The total
256 proportion of MAC was in equilibrium between the two groups (Extended Data Fig. 7b), and
257 integrated analysis of ST profiling showed similar distributions of the three MAC subsets around
258 the scaffold (Fig. 7 j, k). Integrated analysis confirmed the substantial distribution of T cell
259 subsets surrounding the scaffold in both the groups (Fig.7 l, m). In summary, the biomaterial
260 showed similar “pro-regenerative” effect on wound healing despite the wound size. In addition,

261 this resemblance to the immunoregulatory effect of the adaptive immune system indicates a
262 significant role of modulating the immune environment in HF regeneration.

263 **Discussion**

264 Synthetic graft transplantation is an efficient treatment for severe large-area skin wounds,
265 especially when the donor site is not qualified [2]. With additional understanding of tissue
266 engineering, it is suggested that synthetic biomaterials imitating the native structure of ECM can
267 integrate and potentially play a pro-regenerative role in wound healing [4,39].The reconstruction of
268 dermal appendages is an important indicator of full skin regeneration. Nevertheless, existing
269 treatment can only form epidermal or dermal layers and fail to regenerate enough HF and SG[8].
270 Requirements for promotion of nascent HF formation bring significant challenges to biomaterial
271 design, particularly for large-scale severe wounds.

272 Here, the pro-regenerative influence of the adaptive immune system in coordinating the early
273 stages of wound repair has been stressed [40]. We employed an ECM scaffold for large-area skin
274 defects and investigated its immunoregulatory mechanism in wound healing. The scaffold
275 showed an impact by accelerating wound closure and promoting nascent HF formation (Fig. 1 e,
276 g). By multimodal analysis, we observed that substantial T cell infiltration in response to scaffold
277 implantation was driven towards regenerative subpopulations (Fig. 2e, 3h), overlapping with the
278 abundant PF (related to HF regeneration) (Fig. 3d). The local intercellular communications
279 among the enlarged "pro-regenerative" immune niche and HF precursor cells suggested the
280 essential role of the adaptive system in biomaterial-mediated wound regeneration (Fig. 4b). We
281 next confirmed the requirement of T cells in skin regeneration by an immunodeficient model
282 (Fig. 5). These data validated that HF can be reconstructed through the activation adaptive
283 immune by ECM scaffolds. Meanwhile, mild FBR around the scaffold decreased the risk of

284 immune rejection, and the appropriate degradation rate could also avoid the extra expense of
285 secondary surgery in both small and large area wound healing (Fig. 7).
286 In this study, we offered an available manner for large-area wound regeneration and firstly
287 defined the spatial heterogeneity of microenvironment during biomaterial-mediated wound
288 healing process. These techniques provide a unique medium through which we can further
289 understand the immunoregulatory mechanisms of the ECM scaffold. Of note, we testified the
290 role of adaptive immune system activated by biomaterials in HF reconstruction and provides
291 further insights into the future design of targeted immunoregulatory materials for scarless wound
292 regeneration.

293 **Online Methods**

294 **Fabrication of ECM scaffolds**

295 The preparation of ECM scaffolds was similar to previous report[7].To fabricate the
296 electrospinning scaffold with approximate 300nm diameter aligned fibers, 20% w/v PLGA
297 (LA/GA = 75:25, molecular weight = 105 kDa, Jinan Daigang Biomaterial Co. Ltd.) and 2% w/v
298 FC (Sangon Biotech Co. Ltd.) were dissolved in HFIP (Aladdin Co., Ltd.) with stirring until
299 complete dissolution. The solution was fed at 0.018mm/min, and a voltage of -2/5kv and 11 cm
300 distance between the needle (21G) and the rotating cylinder (2800 rpm) was applied. After been
301 dried in a vacuum oven for a week, The morphology of PLGA/FC nanofibrous scaffold was
302 observed by the scanning electron microscopy (SEM; JSM-7500F, JEOL, Japan). The scaffolds
303 were cut into circular shape (0.8cm or 1.8cm in diameter) and sterilized using γ-irradiation
304 before the animal implantation experiments.

305 **Excisional wound model and implantation procedures**

306 All procedures involving animals were approved by the Institution Review Board of West China
307 Hospital of Stomatology (No. WCHSIRB-D-2017-033-R1). C57BL/6J mice (Dossy
308 Experimental Animals Co., Ltd.) and immunodeficient C57Bl/6 (B6.129-Rag2tm1) mice
309 (Shanghai Model Organisms Center Inc., Shanghai, China), at the age of 6 week (~20 g) were
310 used in this research. To minimize wound contraction by the panniculus carnosus of rodents and
311 allow wound healing through the granulation and re-epithelialization like the human skin, we use

312 the mice splinted model[16]. The circular (diameter =0.6 or 1.5cm) full-thickness wound were
313 created in the mice dorsal skin and stented by silicone loops. The mice in further study were
314 divided into three groups: large wound (diameter = 1.5cm) treated with saline (Ctrl_LW) or
315 ECM scaffolds below the wound (ECM_LW), and small wound (diameter = 0.6cm) treated with
316 ECM scaffolds (ECM_SW). Subsequently, the wounds were covered with sterile Tegaderm film
317 (3M) and respectively fixed on the small (inner diameter 8 mm and outer diameter 12 mm, for
318 small wound) or large (inner diameter 18 mm and outer diameter 22 mm, for large wound)
319 silicone ring with uniform suture. Mice were euthanatized at 1, 2, 3, and 4 weeks after the
320 surgery, and the small (diameter 10 mm, for small wound) or large (diameter 25 mm, for large
321 wound) round full-thickness sample was harvested.

322 **Bulk RNA sequencing**

323 Three replicates of mice skin wounds in each group were collected for the of bulk-tissue RNA
324 sequencing procedure. Total amounts and integrity of RNA were assessed using the RNA Nano
325 6000 Assay Kit of the Bioanalyzer 2100 system (Agilent Technologies, CA, USA). mRNA was
326 purified from total RNA by using poly-T oligo-attached magnetic beads. The library fragments
327 were purified with AMPure XP system (Beckman Coulter, Beverly, USA). The PCR
328 amplification product was purified by AMPure XP beads. After the library is qualified by qRT-
329 PCR, the different libraries are pooling and being sequenced by the Illumina NovaSeq 6000.
330 FeatureCounts (v1.5.0-p3) was used to count the reads numbers mapped to each gene. And then
331 FPKM of each gene was calculated based on the length of the gene and reads count mapped to
332 this gene. Differential expression analysis of two groups (three biological replicates per group)
333 was performed using the DESeq2 R package (1.20.0), p−value <0.05 and $|\log_2(\text{foldchange})| > 1$
334 was set as the threshold for significantly differential expression. GO terms and KEGG pathways
335 with corrected P-value less than 0.05 were considered significantly enriched by differential
336 expressed genes.

337 **Single cell RNA sequencing**

338 Specimen harvest procedure for scRNA-seq was like previous report[6],3~4 fresh samples were
339 collected per group. In brief, the wound tissues were firstly digested by the Epidermis
340 Dissociation Kit (Epidermis Dissociation Kit, mouse; Miltenyi Biotec) for enzymatic epidermal-
341 dermal separation. The epidermis part was dissociated by a gentleMACS Dissociator (Miltenyi),
342 then filtered (70-mm cell strainer, Corning, Durham), centrifuged (300g, 10 min, 4°C), and
343 resuspended with phosphate-buffered saline (PBS) containing 0.5% bovine serum albumin

344 (BSA). The dermis part was cut into 1 mm width pieces and mixed with mixed enzyme solution
345 containing type I collagenase (Gibco, Grand Island) and trypsin (Gibco, Canada), then
346 dissociated by gentleMACS Dissociator (Miltenyi), and digested for 2.5 hours in a hybridization
347 oven (Peqlab PerfectBlot). After being dissociated, filtered, centrifuged, and resuspended in red
348 blood cell lysis buffer (Solarbio), the dermis cells were mixed with epidermis part. Then the dead
349 cells and debris were removed by Dead Cell Removal MicroBeads (Miltenyi). Lastly, these
350 suspensions were then carried out for Single-Cell RNA-seq (10x Genomics Chromium Single
351 Cell Kit). Sequencing (10x Genomics Chromium Single Cell 3′ v3) was performed using an
352 Illumina 1.9 mode. Then, reads were aligned, and expression matrices were generated for
353 downstream analysis (Cell Ranger pipeline software). Filtering, normalization, scaling and
354 canonical correlation analysis were performed (Seurat 4.1.2.) for integrated datasets. CellChat
355 was used to predict receptor-ligand probability among cell subpopulations.

356 **Spatial Transcriptomics**

357 Fresh samples were rapidly harvested and frozen in OCT. Wound tissues were cryosectioned at -
358 20 degrees onto gene expression slides. Tissue sections on the Capture Areas of the Visium
359 Spatial Gene Expression are fixed using methanol, H&E staining images will be used
360 downstream to map the gene expression patterns. Using the Visium Tissue Optimization Slide &
361 Reagent kit, permeabilization time was optimized. Second Strand Mix is added to the tissue
362 sections to initiate second strand synthesis. After transfer of cDNA from the slide, spatially
363 barcoded, full-length cDNA is amplified via PCR to generate sufficient mass for library
364 construction. The final libraries contain the P5 and P7 primers used in Illumina amplification. A
365 Visium Spatial Gene Expression library comprises standard Illumina paired-end constructs
366 which begin and end with P5 and P7.Raw FASTQ files and histology images were processed
367 (SpaceRanger software) for genome alignment. Raw output files for each group were read into R
368 studio (Seurat 4.1.2). Normalization across spots was performed with the SCTransform function.
369 The spatial cluster gene signature overlap correlation matrix was generated by first taking all
370 genes differentially expressed (avg_log2FC > 1 and adjusted p value < 0.05) across all ST
371 clusters. Pearson correlation was calculated across this matrix and hierarchical clustering of ST
372 clusters was performed with the heatmap function with the ggplots package. Signature scoring
373 derived from scRNA-seq and ST signatures was performed with the AddModuleScore function.

374 **Histopathology, Immunohistochemistry, and immunofluorescence microscopy**

375 The samples were fixed with 4% paraformaldehyde at least 48 hours before ethanol and xylene
376 dehydration. H&E staining and Masson's trichrome staining were performed for the observation
377 of re-epithelialization and collagen fiber deposition. Immunofluorescence staining for
378 cytokeratin 5 (ab52635, Abcam, 1:200) and cytokeratin 10 (ab76318, Abcam, 1:150) and was
379 performed for to assess keratinization. For the evaluation the infiltration of immune cells,
380 immunohistochemistry staining for CD3 (14-0032-82, Thermo Fisher Scientific, 1:100), CD68
381 (ab283654, Abcam, 1:100), Ly6G (ab238132, Abcam, 1:2000) and immunofluorescent staining
382 for CD3 (14-0032-82, Thermo Fisher Scientific, 1:100), CD68 (ab201844, Abcam, 1:250) were
383 performed.

384 **Flow cytometry analysis**

385 The surface markers of T cells (CD3), monocyte, and macrophages (CD11b, CD68) were
386 examined using flow cytometry to quantification the infiltration of immune cells. The digested
387 cell solutions were coincubated with antibodies against CD68 (Allophycocyanin, ab221251,
388 Abcam), CD3 (fluorescein isothiocyanate, catalog no. 100203, BioLegend), and CD11b
389 (PerCP/Cy5.5, catalog no. ab210299, Abcam) at 1:400 dilution for 30~60 min at 4°C in the dark
390 (100 μl per antibody per sample). Before the staining of CD3, cells were preincubated with
391 purified anti-CD16/CD32 antibody (catalog no. 101301, BioLegend) (1.0 μg per 10^6 cells in 100
392 μl volume) for 5 to 10 min to block Fc receptors. Flow cytometry analysis was performed using
393 Attune Nxt flow cytometer (Thermo Fisher Scientific) and FlowJo 10.8.1. The experiments were
394 performed three times independently (n = 3).

395 **Statistics and reproducibility**

396 At least three independent replicates were conducted to obtain repeatable data, and the data was
397 dealt with Case Viewer software, Image J software, and Prism 8.0 software. Statistical analyses
398 were performed by Student's t-test or one-way analysis of variance (ANOVA) with Tukey post-
399 hoc test. The numerical data are presented as mean ± standard deviation. A value of $p < 0.05$ was
400 considered statistically significant (*$p < 0.05$, **$p < 0.01$, ***$p < 0.001$), and ns means no
401 statistically significant difference.

402 **References and Notes**

403 1 Willyard, C. Unlocking the secrets of scar-free skin healing. *Nature* **563**, S86-s88,
404 doi:10.1038/d41586-018-07430-w (2018).
405 2 Henn, D. *et al.* Xenogeneic skin transplantation promotes angiogenesis and tissue
406 regeneration through activated Trem2(+) macrophages. *Science advances* **7**, eabi4528,
407 doi:10.1126/sciadv.abi4528 (2021).

3 Kurita, M. *et al.* In vivo reprogramming of wound-resident cells generates skin epithelial tissue. *Nature* **561**, 243-247, doi:10.1038/s41586-018-0477-4 (2018).
4 Yi, B., Xu, Q. & Liu, W. An overview of substrate stiffness guided cellular response and its applications in tissue regeneration. *Bioactive materials* **15**, 82-102, doi:10.1016/j.bioactmat.2021.12.005 (2022).
5 Sadtler, K. *et al.* Design, clinical translation and immunological response of biomaterials in regenerative medicine. *Nature Reviews Materials* **1**, 16040, doi:10.1038/natrevmats.2016.40 (2016).
6 Hu, C. *et al.* Dissecting the microenvironment around biosynthetic scaffolds in murine skin wound healing. *Science advances* **7**, doi:10.1126/sciadv.abf0787 (2021).
7 Wang, C. *et al.* The diameter factor of aligned membranes facilitates wound healing by promoting epithelialization in an immune way. *Bioactive materials* **11**, 206-217, doi:10.1016/j.bioactmat.2021.09.022 (2022).
8 Mascharak, S. *et al.* Preventing Engrailed-1 activation in fibroblasts yields wound regeneration without scarring. *Science (New York, N.Y.)* **372**, doi:10.1126/science.aba2374 (2021).
9 Sommerfeld, S. D. *et al.* Interleukin-36γ-producing macrophages drive IL-17-mediated fibrosis. *Science immunology* **4**, doi:10.1126/sciimmunol.aax4783 (2019).
10 Cherry, C. *et al.* Computational reconstruction of the signalling networks surrounding implanted biomaterials from single-cell transcriptomics. *Nature biomedical engineering* **5**, 1228-1238, doi:10.1038/s41551-021-00770-5 (2021).
11 Longo, S. K., Guo, M. G., Ji, A. L. & Khavari, P. A. Integrating single-cell and spatial transcriptomics to elucidate intercellular tissue dynamics. *Nature reviews. Genetics* **22**, 627-644, doi:10.1038/s41576-021-00370-8 (2021).
12 Ji, A. L. *et al.* Multimodal Analysis of Composition and Spatial Architecture in Human Squamous Cell Carcinoma. *Cell* **182**, 497-514.e422, doi:10.1016/j.cell.2020.05.039 (2020).
13 Berglund, E. *et al.* Spatial maps of prostate cancer transcriptomes reveal an unexplored landscape of heterogeneity. *Nature communications* **9**, 2419, doi:10.1038/s41467-018-04724-5 (2018).
14 Gao, S. *et al.* Identification of HSC/MPP expansion units in fetal liver by single-cell spatiotemporal transcriptomics. *Cell research* **32**, 38-53, doi:10.1038/s41422-021-00540-7 (2022).
15 Foster, D. S. *et al.* Integrated spatial multiomics reveals fibroblast fate during tissue repair. *Proceedings of the National Academy of Sciences of the United States of America* **118**, doi:10.1073/pnas.2110025118 (2021).
16 Galiano, R. D., Michaels, J. t., Dobryansky, M., Levine, J. P. & Gurtner, G. C. Quantitative and reproducible murine model of excisional wound healing. *Wound repair and regeneration : official publication of the Wound Healing Society [and] the European Tissue Repair Society* **12**, 485-492, doi:10.1111/j.1067-1927.2004.12404.x (2004).
17 Ito, M. *et al.* Wnt-dependent de novo hair follicle regeneration in adult mouse skin after wounding. *Nature* **447**, 316-320, doi:10.1038/nature05766 (2007).
18 Plikus, M. V. *et al.* Regeneration of fat cells from myofibroblasts during wound healing. *Science (New York, N.Y.)* **355**, 748-752, doi:10.1126/science.aai8792 (2017).
19 Driskell, R. R. *et al.* Distinct fibroblast lineages determine dermal architecture in skin development and repair. *Nature* **504**, 277-281, doi:10.1038/nature12783 (2013).

454 20 Mok, K. *et al.* Dermal Condensate Niche Fate Specification Occurs Prior to Formation
455 and Is Placode Progenitor Dependent. *Developmental cell* **48**, 32-48.e35,
456 doi:10.1016/j.devcel.2018.11.034 (2019).
457 21 Wang, X. *et al.* Macrophages induce AKT/β-catenin-dependent Lgr5(+) stem cell
458 activation and hair follicle regeneration through TNF. *Nature communications* **8**, 14091,
459 doi:10.1038/ncomms14091 (2017).
460 22 Abbasi, S. *et al.* Distinct Regulatory Programs Control the Latent Regenerative Potential
461 of Dermal Fibroblasts during Wound Healing. *Cell stem cell* **27**, 396-412.e396,
462 doi:10.1016/j.stem.2020.07.008 (2020).
463 23 Guerrero-Juarez, C. F. *et al.* Single-cell analysis reveals fibroblast heterogeneity and
464 myeloid-derived adipocyte progenitors in murine skin wounds. *Nature communications*
465 **10**, 650, doi:10.1038/s41467-018-08247-x (2019).
466 24 Rinkevich, Y. *et al.* Skin fibrosis. Identification and isolation of a dermal lineage with
467 intrinsic fibrogenic potential. *Science (New York, N.Y.)* **348**, aaa2151,
468 doi:10.1126/science.aaa2151 (2015).
469 25 Telerman, S. B. *et al.* Dermal Blimp1 Acts Downstream of Epidermal TGFβ and Wnt/β-
470 Catenin to Regulate Hair Follicle Formation and Growth. *The Journal of investigative*
471 *dermatology* **137**, 2270-2281, doi:10.1016/j.jid.2017.06.015 (2017).
472 26 Kim, D. *et al.* Noncoding dsRNA induces retinoic acid synthesis to stimulate hair follicle
473 regeneration via TLR3. *Nature communications* **10**, 2811, doi:10.1038/s41467-019-
474 10811-y (2019).
475 27 Ode Boni, B. O., Lamboni, L., Souho, T., Gauthier, M. & Yang, G. Immunomodulation
476 and cellular response to biomaterials: the overriding role of neutrophils in healing.
477 *Materials Horizons* **6**, 1122-1137, doi:10.1039/C9MH00291J (2019).
478 28 Chu, C. *et al.* Modulation of foreign body reaction and macrophage phenotypes
479 concerning microenvironment. *Journal of biomedical materials research. Part A* **108**,
480 127-135, doi:10.1002/jbm.a.36798 (2020).
481 29 Yu, Y. *et al.* Single-cell RNA-seq identifies a PD-1(hi) ILC progenitor and defines its
482 development pathway. *Nature* **539**, 102-106, doi:10.1038/nature20105 (2016).
483 30 Bielecki, P. *et al.* Skin-resident innate lymphoid cells converge on a pathogenic effector
484 state. *Nature* **592**, 128-132, doi:10.1038/s41586-021-03188-w (2021).
485 31 Shih, H. Y. *et al.* Developmental Acquisition of Regulomes Underlies Innate Lymphoid
486 Cell Functionality. *Cell* **165**, 1120-1133, doi:10.1016/j.cell.2016.04.029 (2016).
487 32 Li, Z. *et al.* Epidermal Notch1 recruits RORγ(+) group 3 innate lymphoid cells to
488 orchestrate normal skin repair. *Nature communications* **7**, 11394,
489 doi:10.1038/ncomms11394 (2016).
490 33 Ebbo, M., Crinier, A., Vély, F. & Vivier, E. Innate lymphoid cells: major players in
491 inflammatory diseases. *Nature reviews. Immunology* **17**, 665-678,
492 doi:10.1038/nri.2017.86 (2017).
493 34 Chang, D. T., Colton, E. & Anderson, J. M. Paracrine and juxtacrine lymphocyte
494 enhancement of adherent macrophage and foreign body giant cell activation. *Journal of*
495 *biomedical materials research. Part A* **89**, 490-498, doi:10.1002/jbm.a.31981 (2009).
496 35 Ali, N. *et al.* Regulatory T Cells in Skin Facilitate Epithelial Stem Cell Differentiation.
497 *Cell* **169**, 1119-1129.e1111, doi:10.1016/j.cell.2017.05.002 (2017).
498 36 Jin, S. *et al.* Inference and analysis of cell-cell communication using CellChat. *Nature*
499 *communications* **12**, 1088, doi:10.1038/s41467-021-21246-9 (2021).

37 Sadtler, K. *et al.* Developing a pro-regenerative biomaterial scaffold microenvironment requires T helper 2 cells. *Science (New York, N.Y.)* **352**, 366-370, doi:10.1126/science.aad9272 (2016).
38 Doloff, J. C. *et al.* Colony stimulating factor-1 receptor is a central component of the foreign body response to biomaterial implants in rodents and non-human primates. *Nat Mater* **16**, 671-680, doi:10.1038/nmat4866 (2017).
39 Monavarian, M., Kader, S., Moeinzadeh, S. & Jabbari, E. Regenerative Scar-Free Skin Wound Healing. *Tissue engineering. Part B, Reviews* **25**, 294-311, doi:10.1089/ten.TEB.2018.0350 (2019).
40 Wang, G. *et al.* Bacteria induce skin regeneration via IL-1β signaling. *Cell host & microbe* **29**, 777-791.e776, doi:10.1016/j.chom.2021.03.003 (2021).

Acknowledgments: We thank the Novogene company for RNA sequencing work, and the National Clinical Research Center for Oral Diseases & State Key Laboratory of Oral Diseases for animal experiment, and the Analytical & Testing Center of Sichuan University for the fabrication of biomaterials. We thank Chen Hu, Xin-hui Li, Jia-yu Gao and Sheng-an Rung for the help with analysis.

Funding:

National Natural Science Foundation of China grant 81870801 (Y.L.Q.); 81970965 (Y.M.)

Sichuan Science and Technology Plan grant 2022YFS0041 (Y.L.Q.)

Interdisciplinary Innovation Project, West China Hospital of Stomatology Sichuan University grant RD-03- 202006 (Y.M.)

Research and Develop Program, West China Hospital of Stomatology Sichuan University grant LCYJ2019-19 (Y.M.)

Author contributions:

Conceptualization: YY, CCY, YM, LL, YLQ

Methodology: CYC, LL, CBW

Investigation: YY

Visualization: YY

Writing – original draft: YY

Writing – review & editing: CCY

Project administration: CCY

Funding acquisition & Supervision: YM, YLQ

Competing interests: Authors declare that they have no competing interests.

Data and materials availability: All data to support the conclusions in this manuscript can be found in the figures and the supplementary materials. Any other data can be requested from the corresponding authors.

Figures

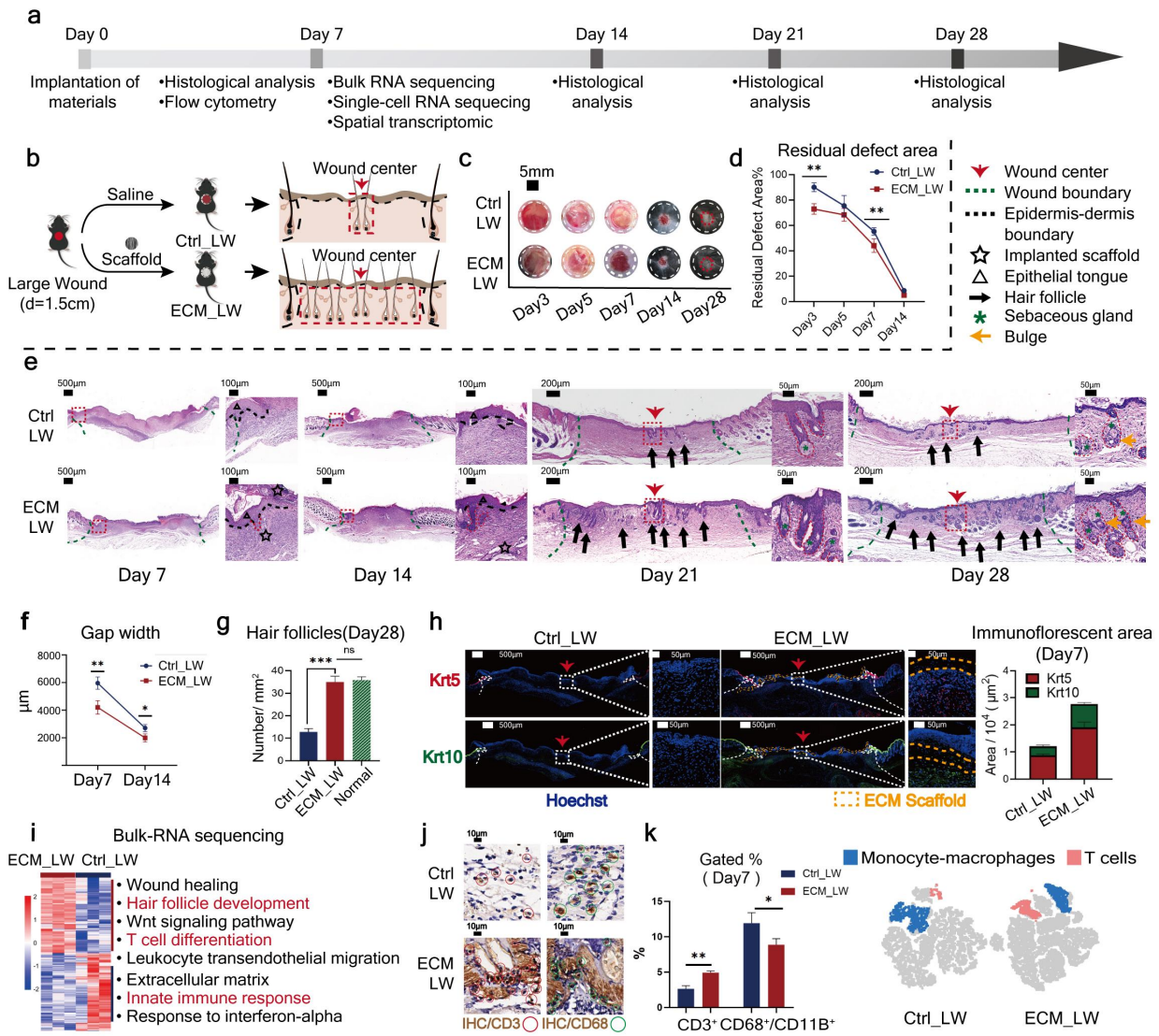

Fig. 1 | Evaluation of the wound healing process treated with ECM scaffolds. (a) Workflow for evaluating large-scale wound healing. (b) Surgical processes for skin excisional wound model. (c) Residual wound area at 3, 5, 7, 14 and 28 days, and (d) corresponding analysis (n=3 for each group). (e) H&E analysis of two groups at 7, 14, 21 and 28 days. (f) semiquantitative evaluation of gap width (n=3 for each group). (g) Histologic quantification of de novo HFs on POD28 (n=3 for each group).(h) IF staining using Krt5 (red) and Krt10 (green), and semiquantitative evaluation of the fluorescent area. (i) Heatmap showing hierarchical clustering of differentially expressed genes (p value<0.05 & |log2FC|> 1) and gene set enrichment analysis (n=3 for each group).(j) IHC staining of CD3 and CD68 at 7 days. (k) In vivo flow cytometry

550 strategy using CD3 to identify T cells, CD68 and CD11b to identify monocyte-macrophages, and
551 visualization of the cells in the tSNE (t-distributed Stochastic Neighbor Embedding) plot. ***P <
552 0.0001, **P < 0.01, and *P < 0.05 by Student's t-test for data in (d), (f),(h) and (k) , and analysis
553 of variance (ANOVA) for data in (g).
554

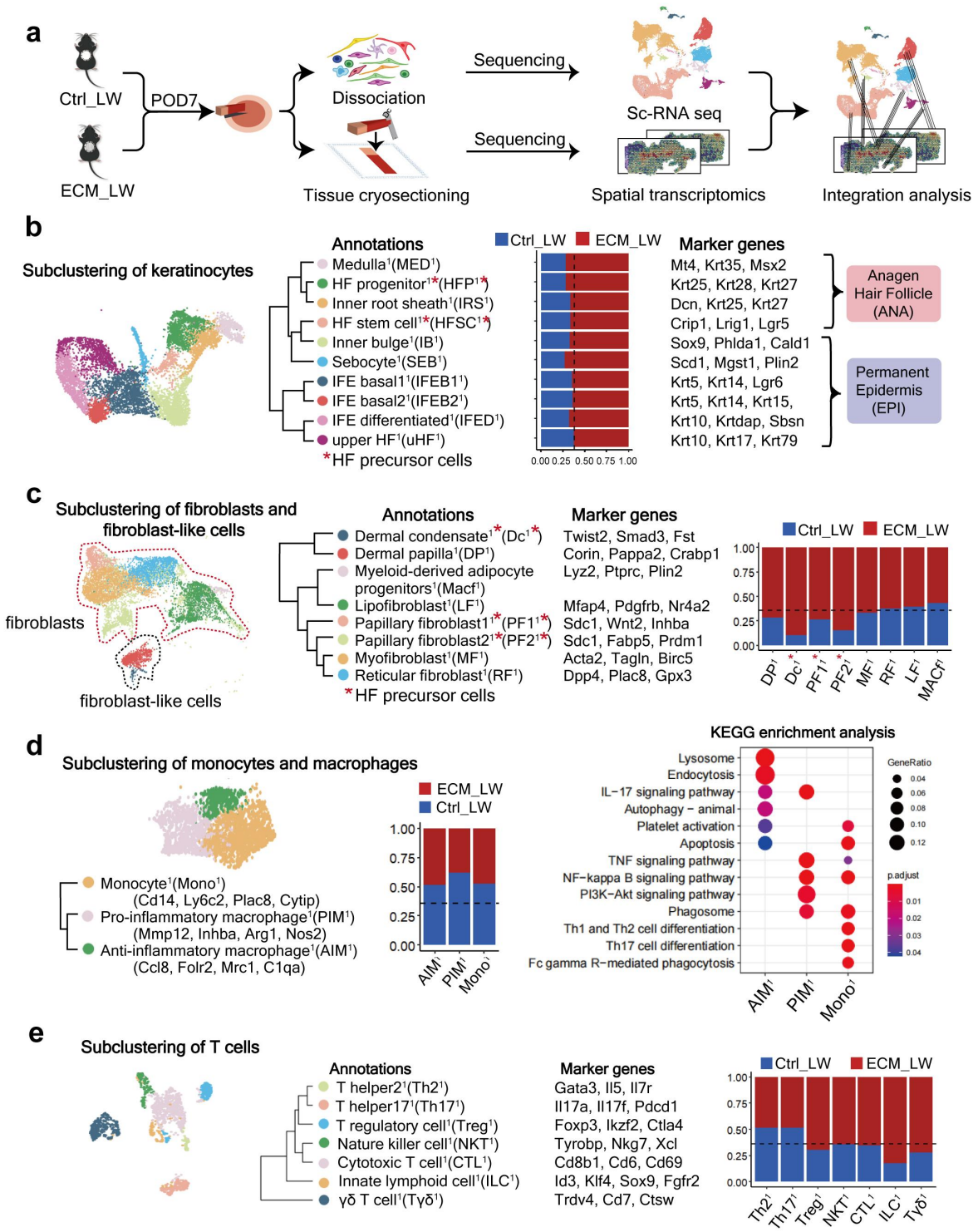

Fig. 2 | The single-cell atlas of biomaterials mediated microenvironment.(a) Schematic for generating scRNA-seq and spatial transcriptomics data from large area excisional wounds. (b) Subclustering of keratinocytes showing four subsets from anagen hair follicle and six subsets from permanent epidermis. The composition and marker genes for each subset are listed. (c)

560 Subclustering of fibroblasts showing two fibroblast-like subsets and six fibroblast subsets. The
561 marker genes and composition for each subset are listed. (d) Subclustering of
562 monocyte/macrophage showing three subsets. The marker genes, composition and KEGG
563 enrichment analysis for each subset are listed. (e) Subclustering of T cells showing seven subsets.
564 The marker genes and composition for each subset are listed.
565

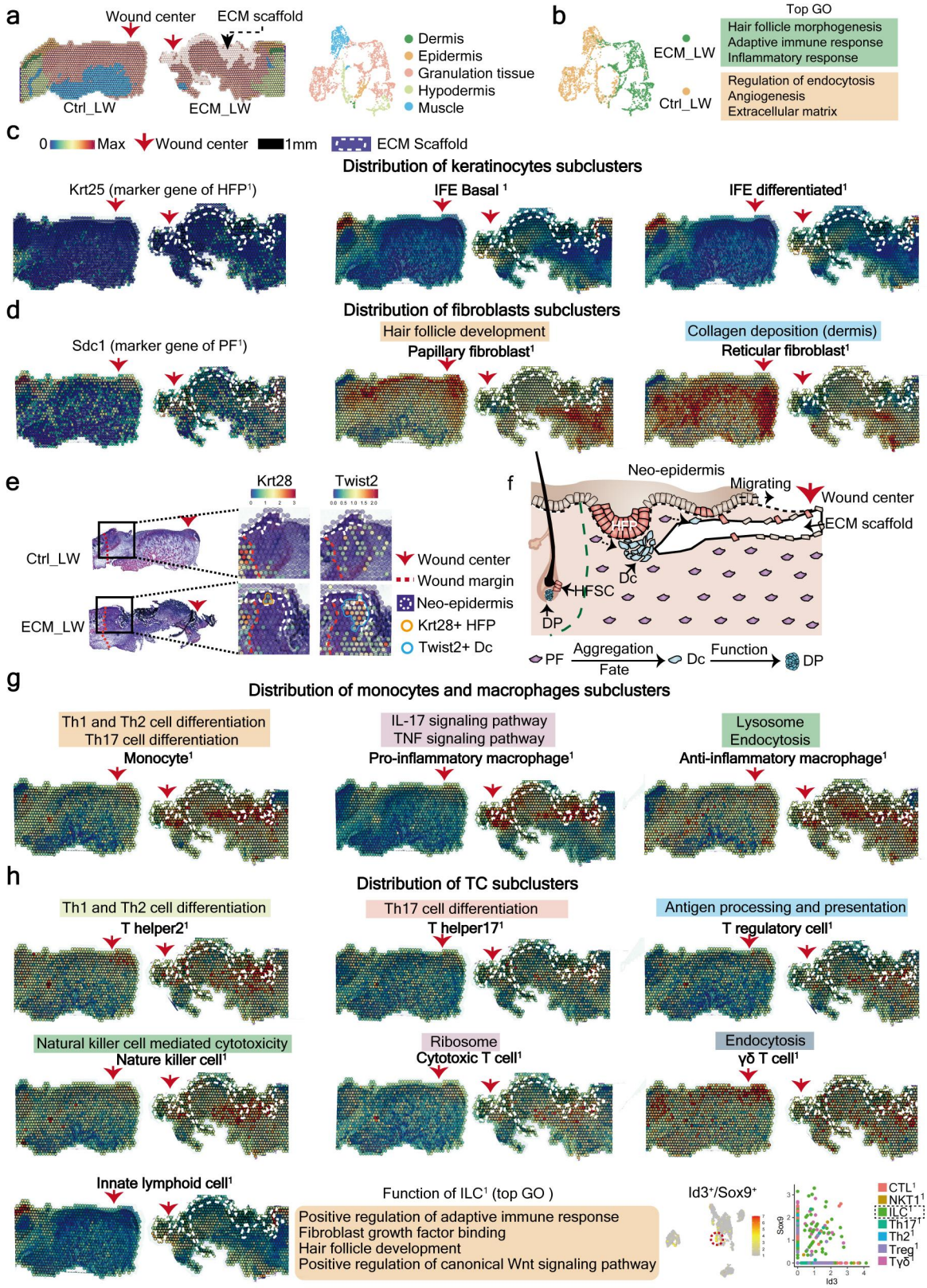
a
Wound center
ECM scaffold
Ctrl_LW
ECM_LW
Dermis
Epidermis
Granulation tissue
Hypodermis
Muscle
b
Top GO
ECM_LW
Ctrl_LW
Hair follicle morphogenesis
Adaptive immune response
Inflammatory response
Regulation of endocytosis
Angiogenesis
Extracellular matrix
c
0 Max
Wound center
1mm
ECM Scaffold
Distribution of keratinocytes subclusters
Krt25 (marker gene of HFP¹)
IFE Basal ¹
IFE differentiated¹
d
Distribution of fibroblasts subclusters
Sdc1 (marker gene of PF¹)
Hair follicle development
Papillary fibroblast¹
Collagen deposition (dermis)
Reticular fibroblast¹
e
Krt28
Twist2
Ctrl_LW
ECM_LW
Wound center
Wound margin
Neo-epidermis
Krt28+ HFP
Twist2+ Dc
f
Neo-epidermis
Migrating
Wound center
ECM scaffold
HFP
Dc
HFSC
DP
PF
Aggregation
Fate
Dc
Function
DP
g
Distribution of monocytes and macrophages subclusters
Th1 and Th2 cell differentiation
Th17 cell differentiation
Monocyte¹
IL-17 signaling pathway
TNF signaling pathway
Pro-inflammatory macrophage¹
Lysosome
Endocytosis
Anti-inflammatory macrophage¹
h
Distribution of TC subclusters
Th1 and Th2 cell differentiation
T helper2¹
Th17 cell differentiation
T helper17¹
Antigen processing and presentation
T regulatory cell¹
Natural killer cell mediated cytotoxicity
Nature killer cell¹
Ribosome
Cytotoxic T cell¹
Endocytosis
γδ T cell¹
Innate lymphoid cell¹
Function of ILC¹ (top GO)
Positive regulation of adaptive immune response
Fibroblast growth factor binding
Hair follicle development
Positive regulation of canonical Wnt signaling pathway
Id3⁺/Sox9⁺
Sox9
Id3
CTL¹
NKT1¹
ILC¹
Th17¹
Th2¹
Treg¹
Tγδ¹

566

567 **Fig. 3 | Spatial anchors tracing the cell distribution around the ECM scaffold.** (a) The
568 unsupervised clustering indicated the anatomical structure of samples. (b) Gene enrichment
569 analysis between ECM_LW and Ctrl_LW group. (c) Spatial feature plot showing the expression
570 of Krt25 (marker gene for hair follicle progenitor) and defined keratinocyte subclusters in tissue
571 sections. (d) Spatial feature plot showing the expression of Sdc1 (marker gene for papillary
572 fibroblast) and defined fibroblast subclusters in tissue sections. (d) Spatial feature plot
573 highlighted the expression of $Krt28^{+}$ hair follicle progenitor and $Twist2^{+}$ dermal condensate in
574 migrating neo-epidermis. (f) Illustration showing the epithelialization along with de novo HF
575 formation in biomaterials mediated healing process. (g) Spatial feature plot showing the
576 expression of defined monocyte, macrophage (MAC) subclusters in tissue sections. (h) Spatial
577 feature plot showing the expression of defined T cell subclusters in tissue sections.
578

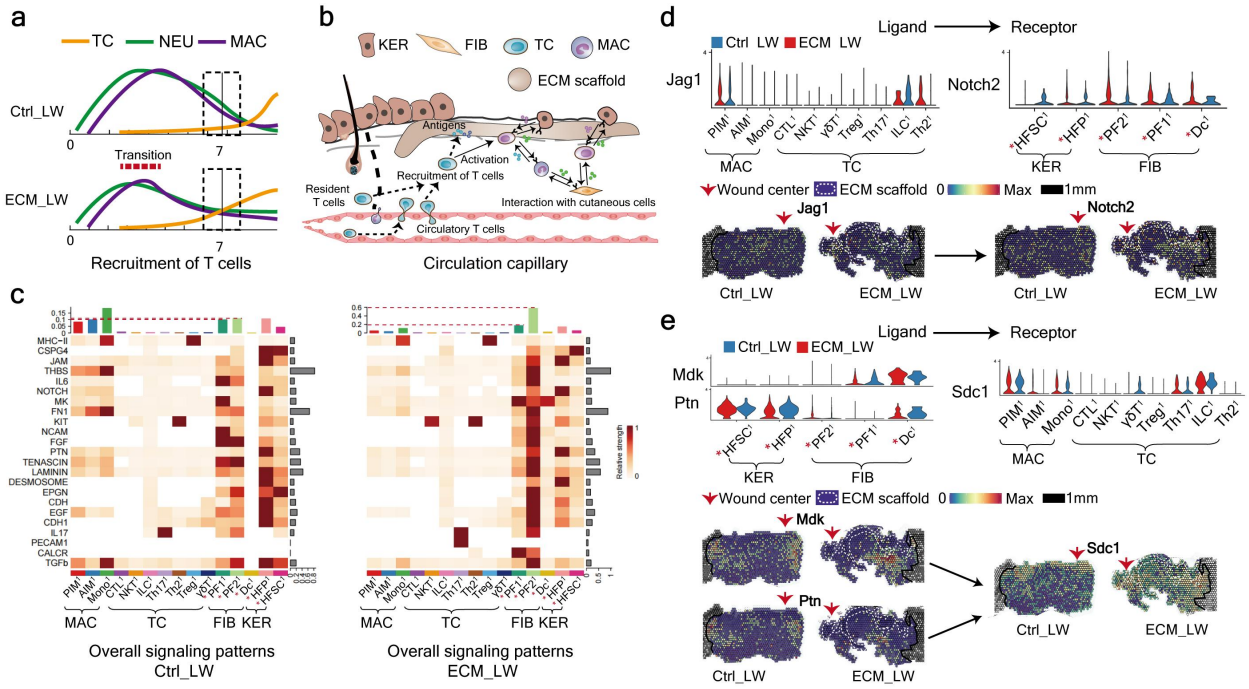

Fig. 4 | Cellular communication landscape between immune cells and cutaneous cells. (a) Schematic timeline highlighting the recruitment of immune cell from innate and adaptive immune systems in Ctrl_LW (top) and ECM_LW (bottom) groups. (b) Schematic of combined ligand-receptor analysis between cutaneous cells and adaptive immune cells in biomaterial treated group. (c) Comparison of overall cell-cell communication patterns between Ctrl_LW and ECM_LW using CellChat. (d) Violin plot (scRNA-seq) and spatial feature plots (ST) showing select ligands and cognate receptor expression of NOTCH signaling pathway. (e) Violin plot (scRNA-seq) and spatial feature plots (ST) showing select ligands and cognate receptor expression of MK and PTN signaling pathways.

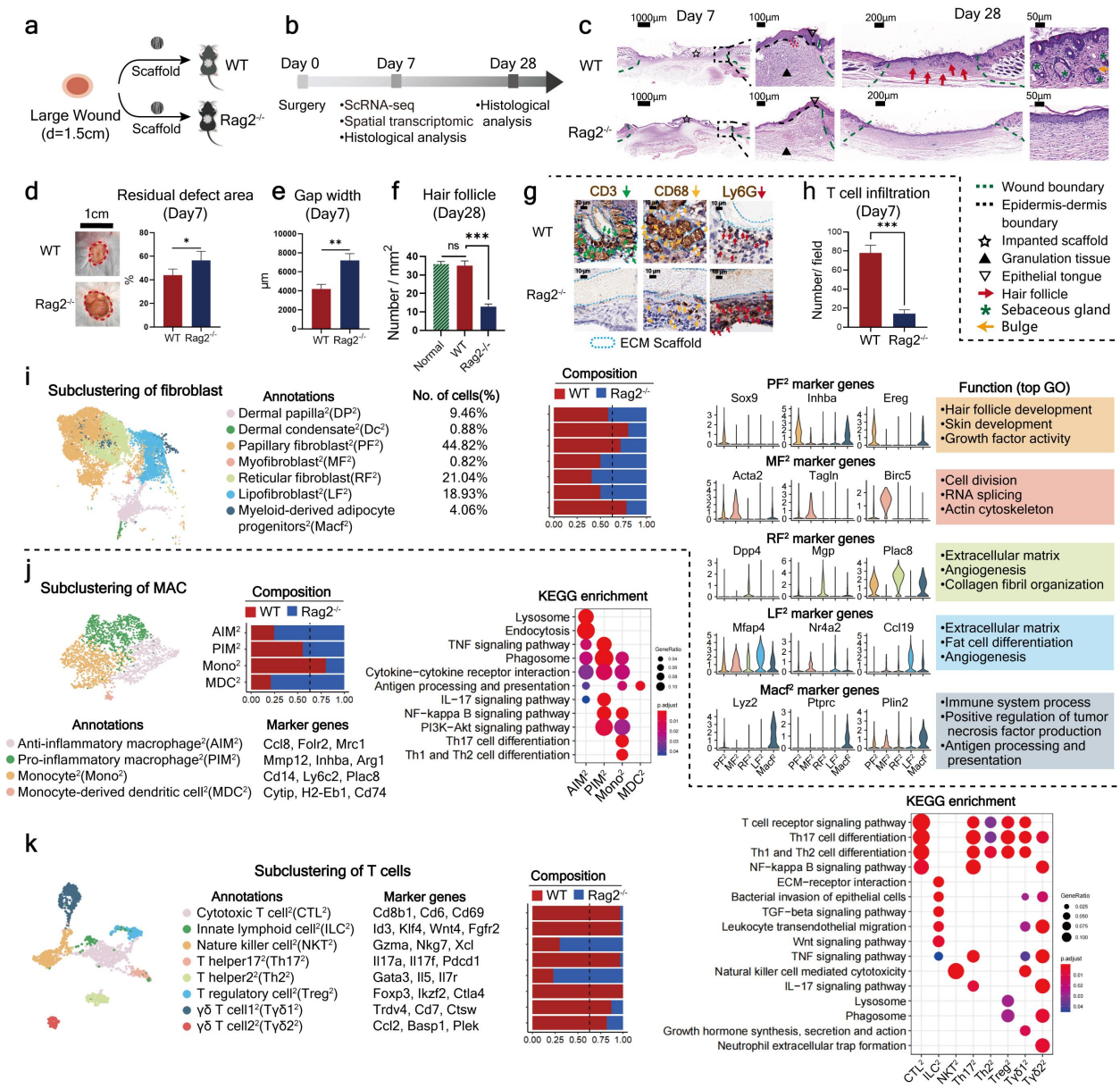

Fig. 5 | Evaluation of wound healing in immunodeficient mice lacking mature T cells.(a) Surgical process and (b) workflow for evaluating large area wound healing mediated by ECM scaffold in WT and Rag2$^{-/-}$ mice. (c) Histological analysis of wound healing in WT and Rag2$^{-/-}$ mice at 7 and 28 days. (d) Residual defect area at 7 days after wound (n=3 for each group). (e) Semiquantitative evaluation of gap width (n=3 for each group). (f) Histologic quantification of de novo HFs (n=3 for each group). (g) IHC staining of CD3 and CD68 and (h) semi-quantification of CD3^{+} T cells infiltration (n=3 for each group). (i) Subclustering of fibroblasts showing two fibroblast-like subsets and five fibroblast subsets. Marker genes for fibroblast

599 subsets and their enriched gene sets in GO analysis are listed. (j) Subclustering of
600 monocyte/macrophage showing four subsets. The marker genes, composition and KEGG
601 enrichment analysis for each subset are listed. (e) Subclustering of T cells showing eight subsets.
602 The marker genes, composition and KEGG enrichment analysis for each subset are listed. ***P
603 < 0.0001, **P < 0.01, and *P < 0.05 by Student's t-test for data in (d), (e) and (h) , and analysis
604 of variance (ANOVA) for data in (f).
605

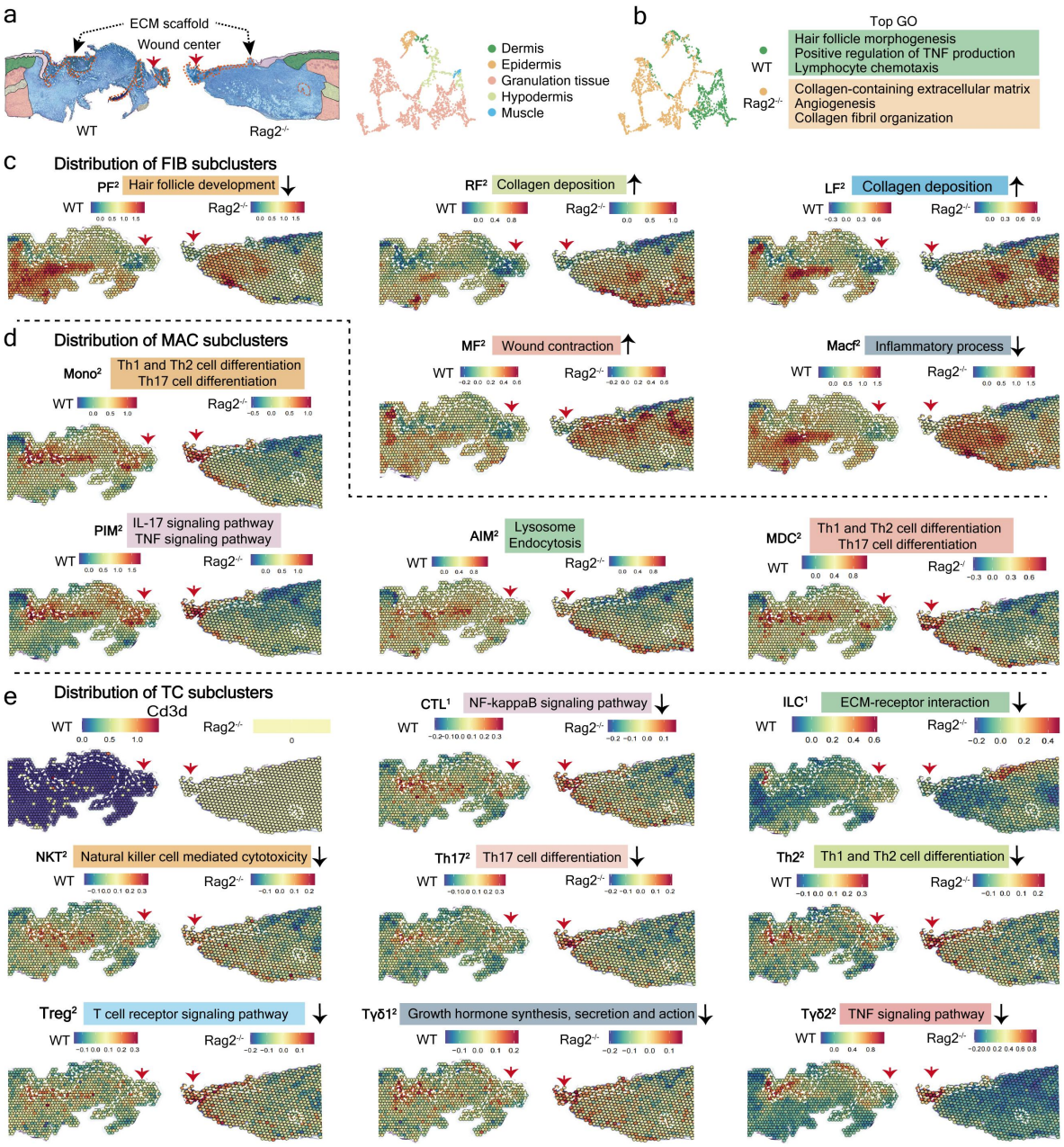

Fig. 6 | Spatial atlas of cell microenvironment around biomaterials of immunodeficient mice. (a) The anatomical structure of each sample which could be distinguished by Seurat. (b) Gene enrichment analysis between WT and Rag2$^{-/-}$ group. (c) Spatial feature plot showing the defined fibroblast subclusters in tissue sections. (d) Spatial feature plot showing the expression of defined monocyte, macrophage (MAC) subclusters in tissue sections. (e) Spatial feature plot showing the expression of defined T cell subclusters in tissue sections.

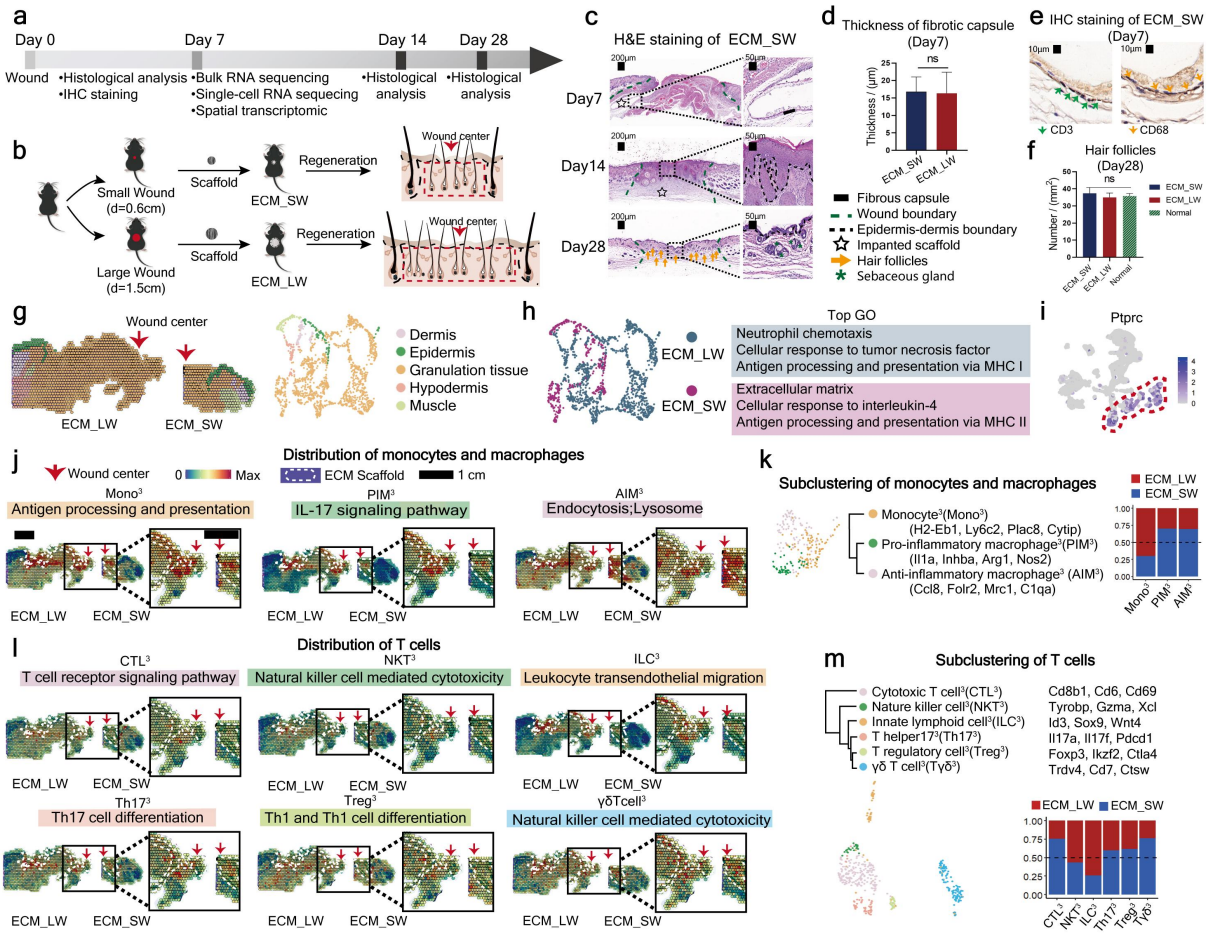

Fig. 7 | Evaluation of the healing of small and large full-thickness wound treated with ECM scaffolds. (a) Workflow for evaluating skin wound healing. (b) Surgical process for skin excisional wound model of ECM_SW and ECM_LW group. (c) H&E staining of ECM_SW samples. (d) Thickness of fibrotic capsule around membrane of ECM_SW and ECM_LW group (n=3 for each group). (e) IHC staining of CD3 and CD68. (f) Histologic quantification of de novo hair follicles on POD28 (n=3 for each group). (g) The unsupervised clustering indicated the anatomical structure of sample. (h) Gene enrichment analysis between ECM_LW and ECM_SW. (i) Feature plot showing the expression of Ptprc (Cd45) in scRNA-seq dataset. (j) Spatial feature plot showing the expression of defined monocyte, macrophage (MAC) subclusters in tissue sections. (k) Subclustering of MAC in sc-RNA seq dataset. (l) Spatial feature plot showing the expression of defined T cell subclusters in tissue sections. (m) Subclustering of T cell in sc-RNA seq dataset. ***P < 0.0001, **P < 0.01, and *P < 0.05 by Student's t-test for data in (d), and analysis of variance (ANOVA) for data in (f).

Extended data

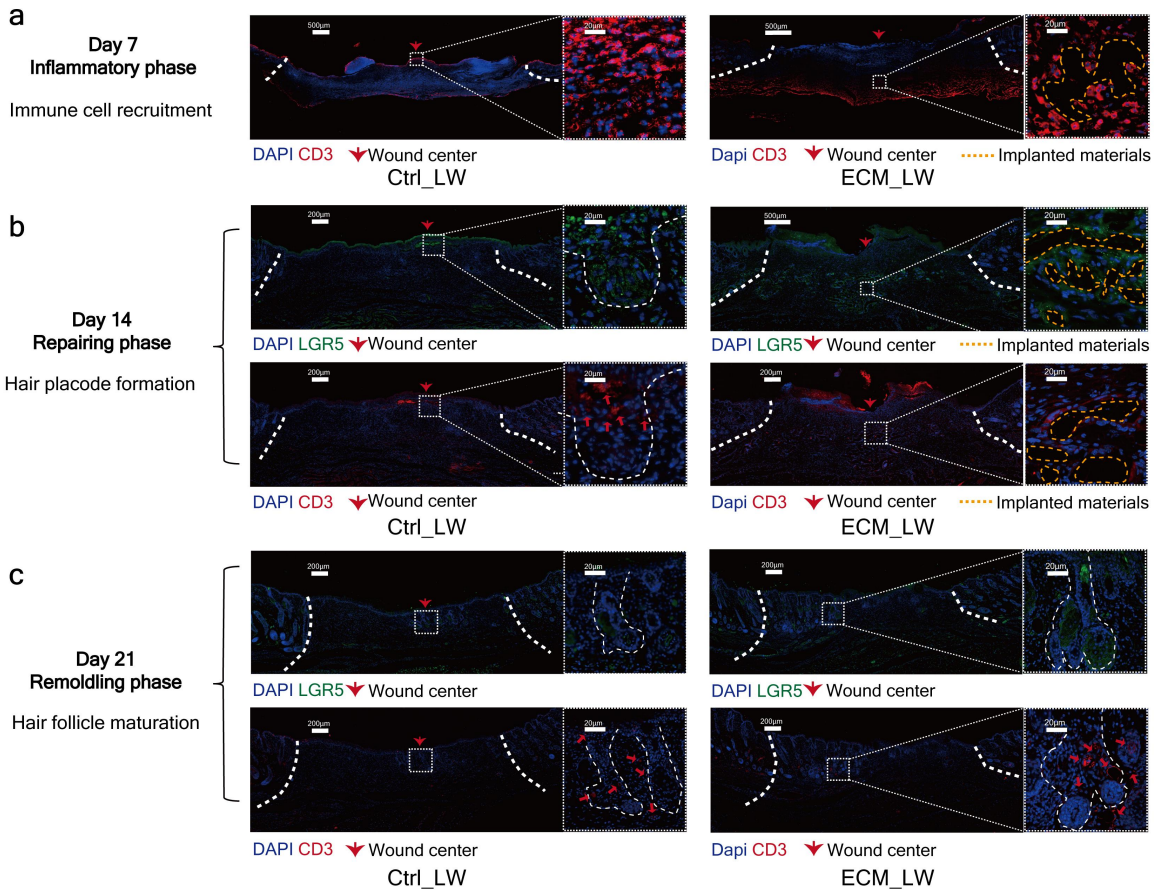

Extended Data Fig. 1 | Evaluation the distribution of the HFSC and T cell. (a) Immunostaining for CD3 (red) showing the significant $CD3^+$ T cell recruitment in biomaterial-implanted group on day 7. (b) Immunostaining for LGR5 (green) and CD3 (red) reveals $LGR5^+$ HFSC and $CD3^+$ T cell infiltration around biomaterials on day 14. (c) Immunostaining for LGR5 (green) and CD3 (red) reveals many $LGR5^+$ HFSC within the bulge region of neogenic hair follicles adjacent to $CD3^+$ T cells on day 21.

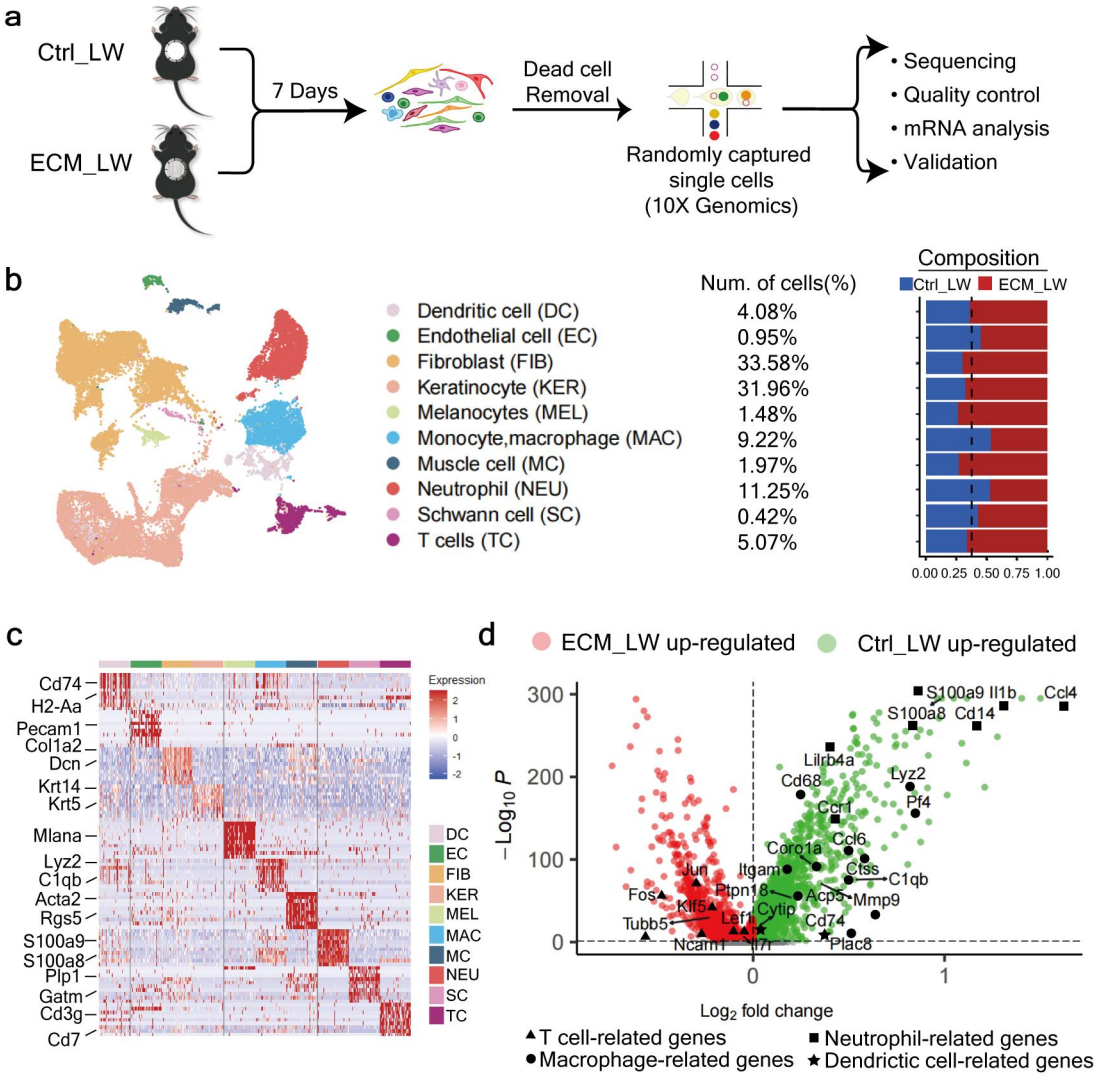

Extended Data Fig. 2 | Overview of the single-cell transcriptome analysis between ECM_LW and Ctrl_LW. (a) Single-cell experiment workflow. (b) Cells are categorized into 10 main clusters. The number of cell populations in each cluster, number of cells (%), and composition of ECM_LW and Ctrl_LW groups are listed. (c) Heatmap showing top10 marker genes for each cluster. (d) Volcano plot showing interested differentially expressed genes in ECM_LW and Ctrl_LW group (scRNA-seq).

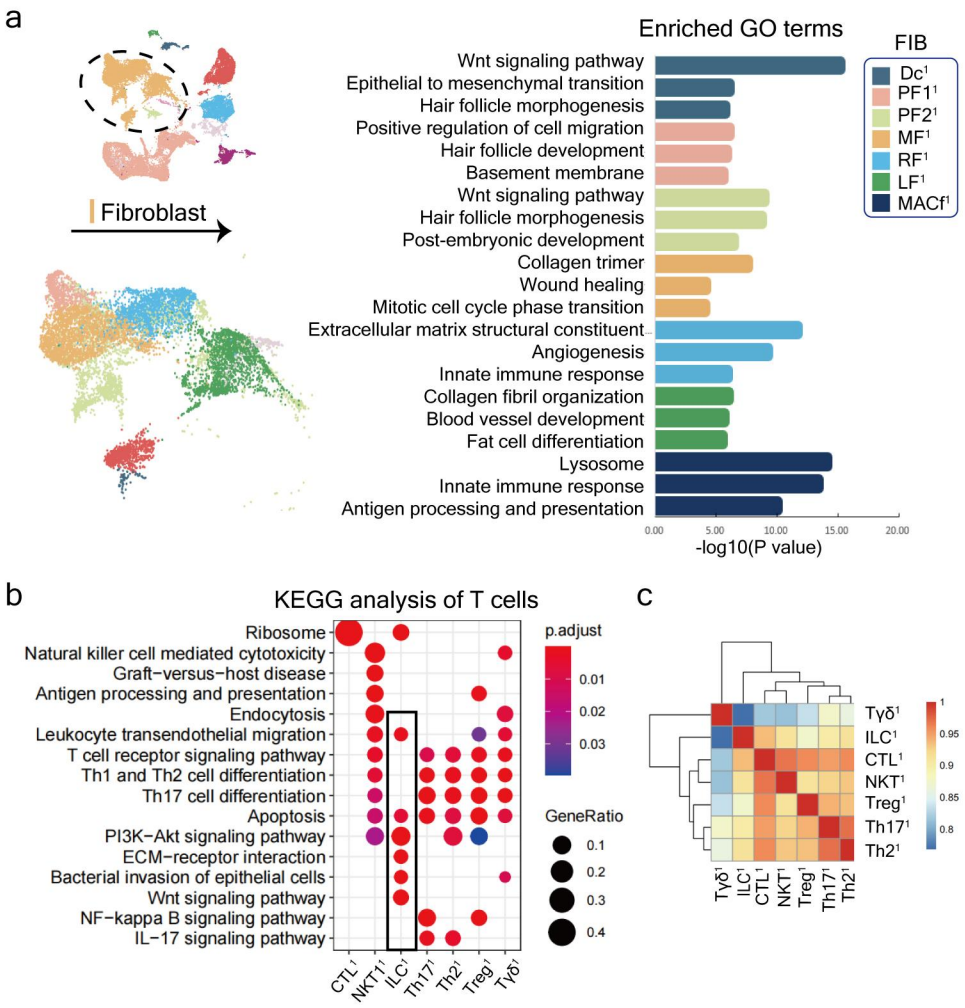

Extended Data Fig. 3 | Further analysis of fibroblasts and T cells between ECM_LW and Ctrl_LW. (a) GO enrichment analysis of fibroblast subtypes. (b) KEGG enrichment analysis of T cell subtypes. (c) Pearson correlation analysis of T cell subsets based on average gene expression.

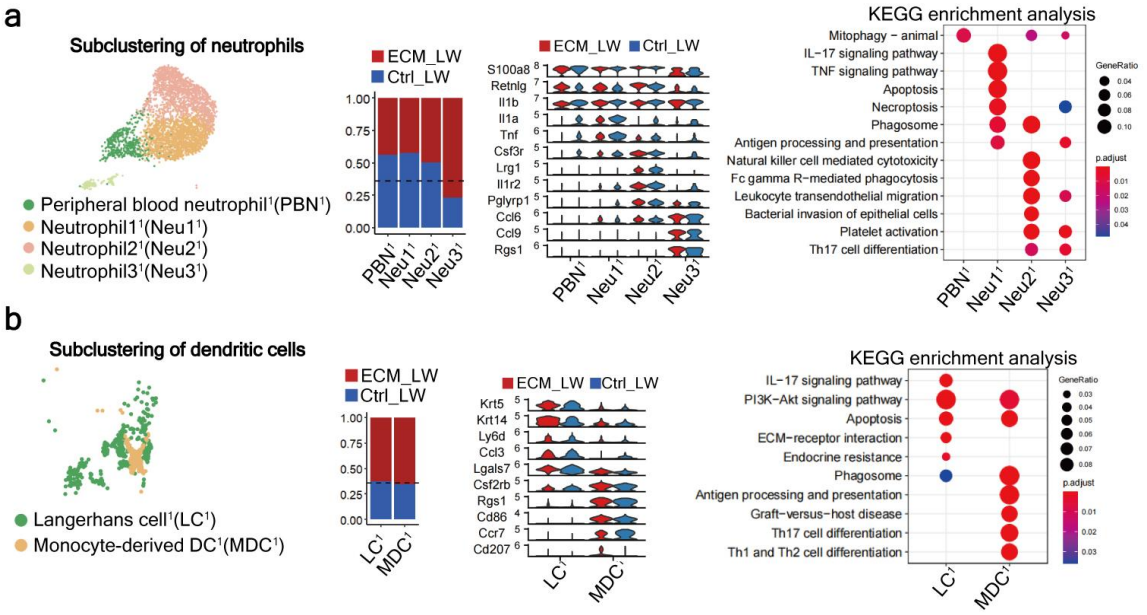

Extended Data Fig. 4 | Subclustering analysis of neutrophils and dendritic cells between ECM_LW and Ctrl_LW. (a) Subclustering of neutrophils showing four subsets. The marker genes, composition and KEGG enrichment analysis for each subset are listed. (b) Subclustering of dendritic cells showing two subsets, marker genes, composition and KEGG enrichment analysis are listed.

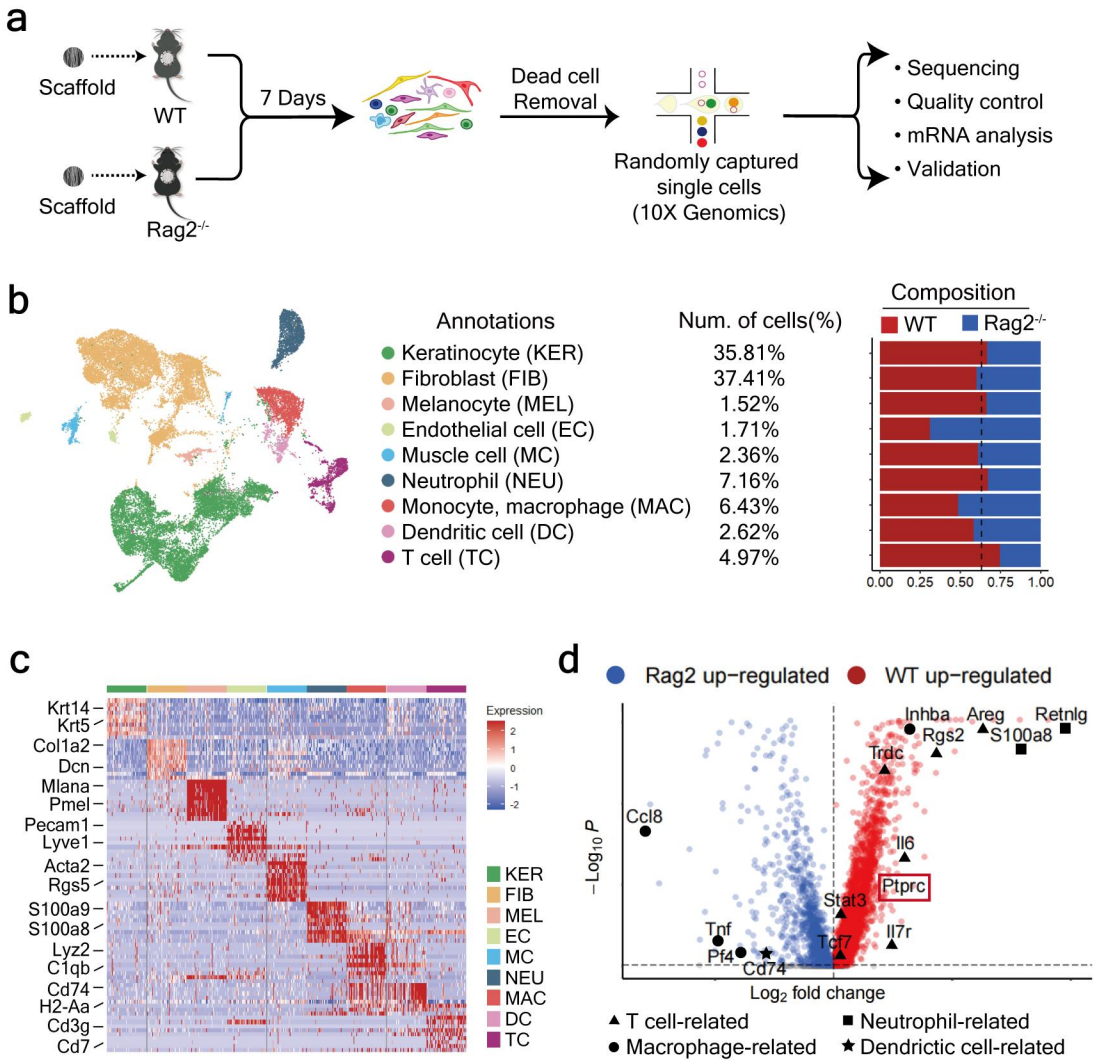

Extended Data Fig. 5 | Overview of the single-cell transcriptome analysis between WT and Rag2$^{-/-}$ mice treated with biomaterials. (a) Single-cell experiment workflow. (b) Cells are categorized into nine main clusters. The number of cell populations in each cluster, number of cells (%), and composition of ECM_LW and Ctrl_LW groups are listed. (C) Heatmap showing top10 marker genes for each cluster. (d) Volcano plot showing interested differentially expressed genes in WT and Rag2$^{-/-}$ group (scRNA-seq).

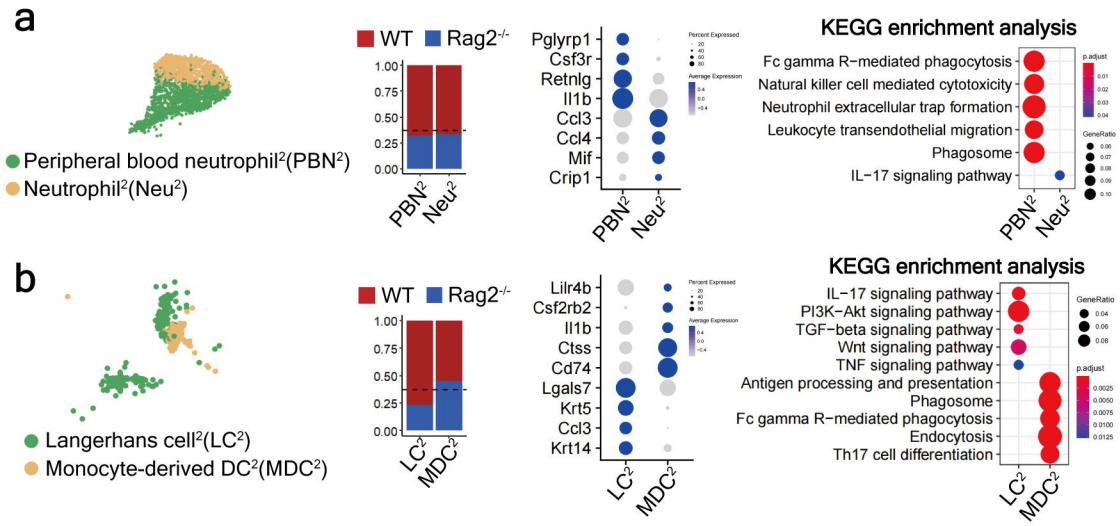

Extended Data Fig. 6 | Subclustering analysis of neutrophils and dendritic cells between WT and Rag2$^{-/-}$ mice (a) Subclustering of neutrophils showing two subsets. The marker genes, composition and KEGG enrichment analysis for each subset are listed. (b) Subclustering of dendritic cells showing two subsets, marker genes, composition and KEGG enrichment analysis are listed.

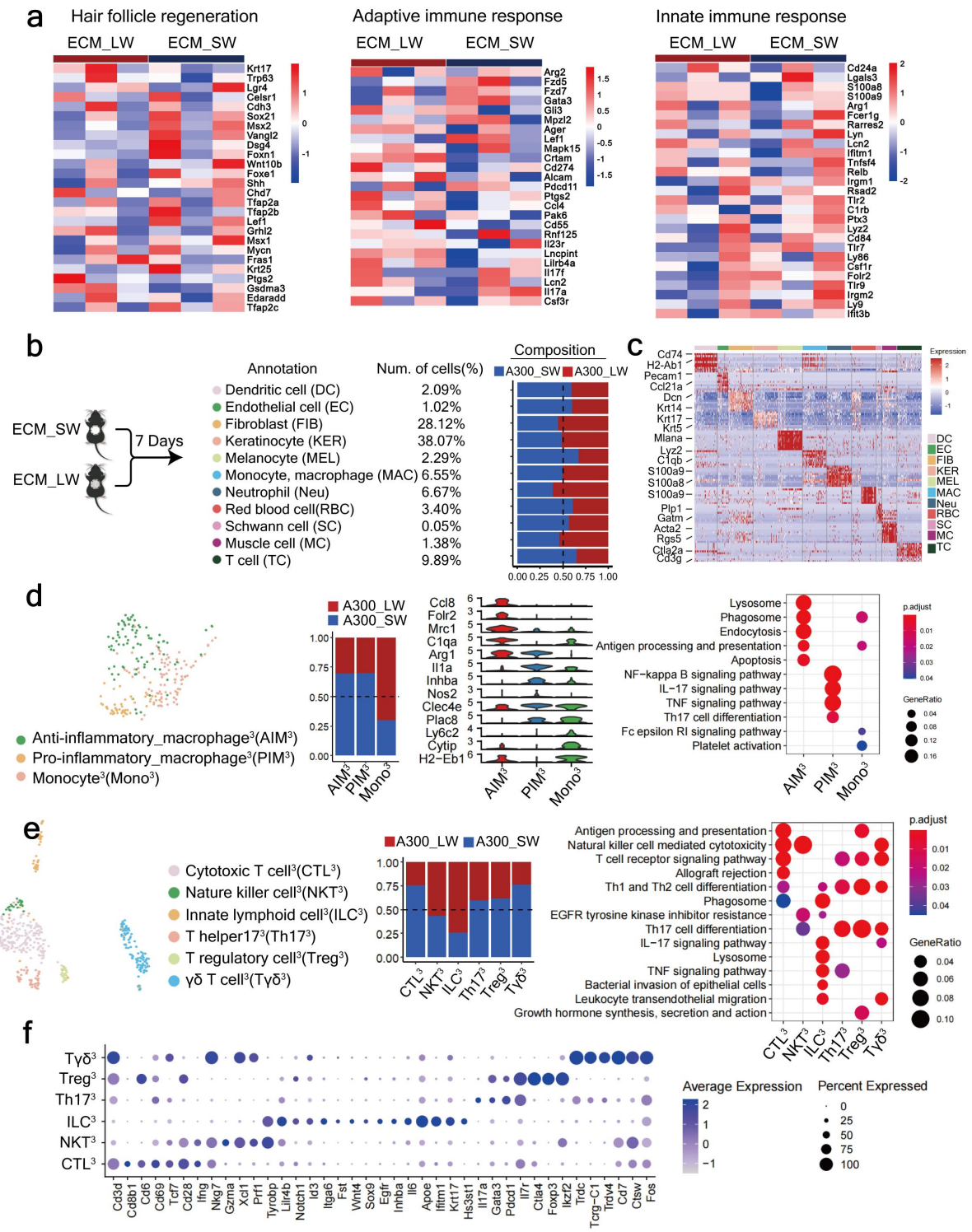

674

675 **Extended Data Fig. 7 | ScRNA-seq and ST analysis between ECM_SW and ECM_LW.** (A)
676 Heatmap showing expression of hair follicle regeneration, adaptive immune response, and innate
677 immune response related genes (bulk seq). (B) Single cells are categorized into 11 main clusters.

678 The number of cell populations in each cluster, number of cells (%), and composition of
679 ECM_LW and ECM_SW groups are listed. (C) Heatmap showing top10 marker genes for each
680 cluster. (D) Subclustering of MAC showing three subsets; The composition for each subset is
681 listed; Marker genes for each MAC subset and enrichment analysis of KEGG pathway. (E)
682 Subclustering of T cells showing seven subsets; The composition for each subset is listed and
683 enrichment analysis of KEGG analysis. (F) Marker genes for T cell subsets.
684
685